Science Advances
AAAS

advances.sciencemag.org/cgi/content/full/6/14/eaaz5004/DC1

Supplementary Materials for

Symmetry breaking in hydrodynamic forces drives meiotic spindle rotation in mammalian oocytes

HaiYang Wang, Yizeng Li, Jing Yang, Xing Duan, Petr Kalab, Sean X. Sun*, Rong Li*

*Corresponding author. Email: ssun@jhu.edu (S.X.S.); rong@jhu.edu (R.L.)

Published 3 April 2020, *Sci. Adv.* **6**, eaaz5004 (2020)
DOI: 10.1126/sciadv.aaz5004

The PDF file includes:

Figs. S1 to S8
Tables S1 to S3
Legends for movies S1 to S14
References

Other Supplementary Material for this manuscript includes the following:

(available at advances.sciencemag.org/cgi/content/full/6/14/eaaz5004/DC1)

Movies S1 to S14

Figure S1

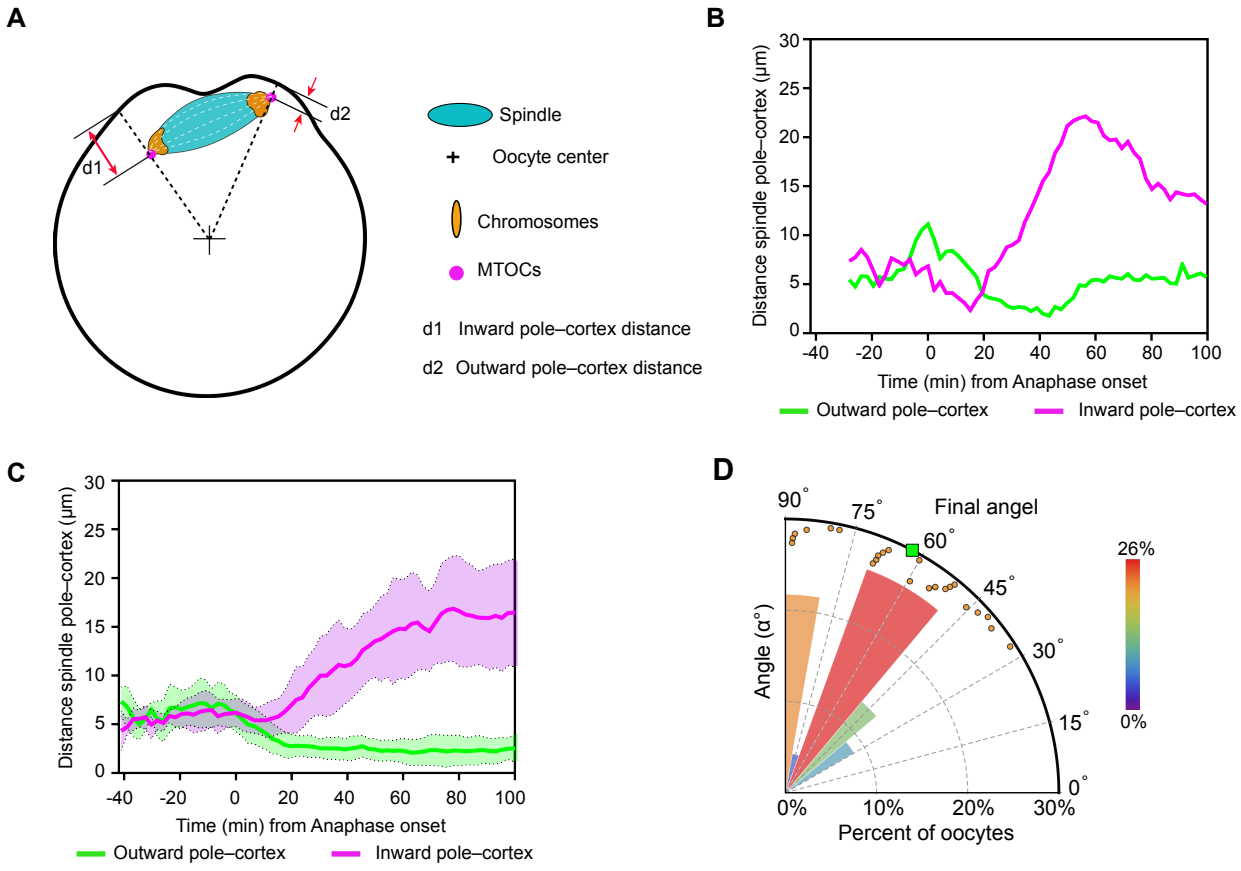

fig. S1. Characterization of spindle rotation in activated MII oocytes.

(A) Diagram indicating the measurements of the distance between spindle pole and oocyte cortex**.** **(B and C)** Distance between each spindle pole and oocyte cortex over time for a single oocyte (B) and averaged values (C) for 15 oocytes (mean ± SD). **(D)** Final angles of spindle rotation in 23 oocytes observed. The color code showed the percent of oocytes. Green square, mean value; orange dots, individual spindle angles.

Figure S2

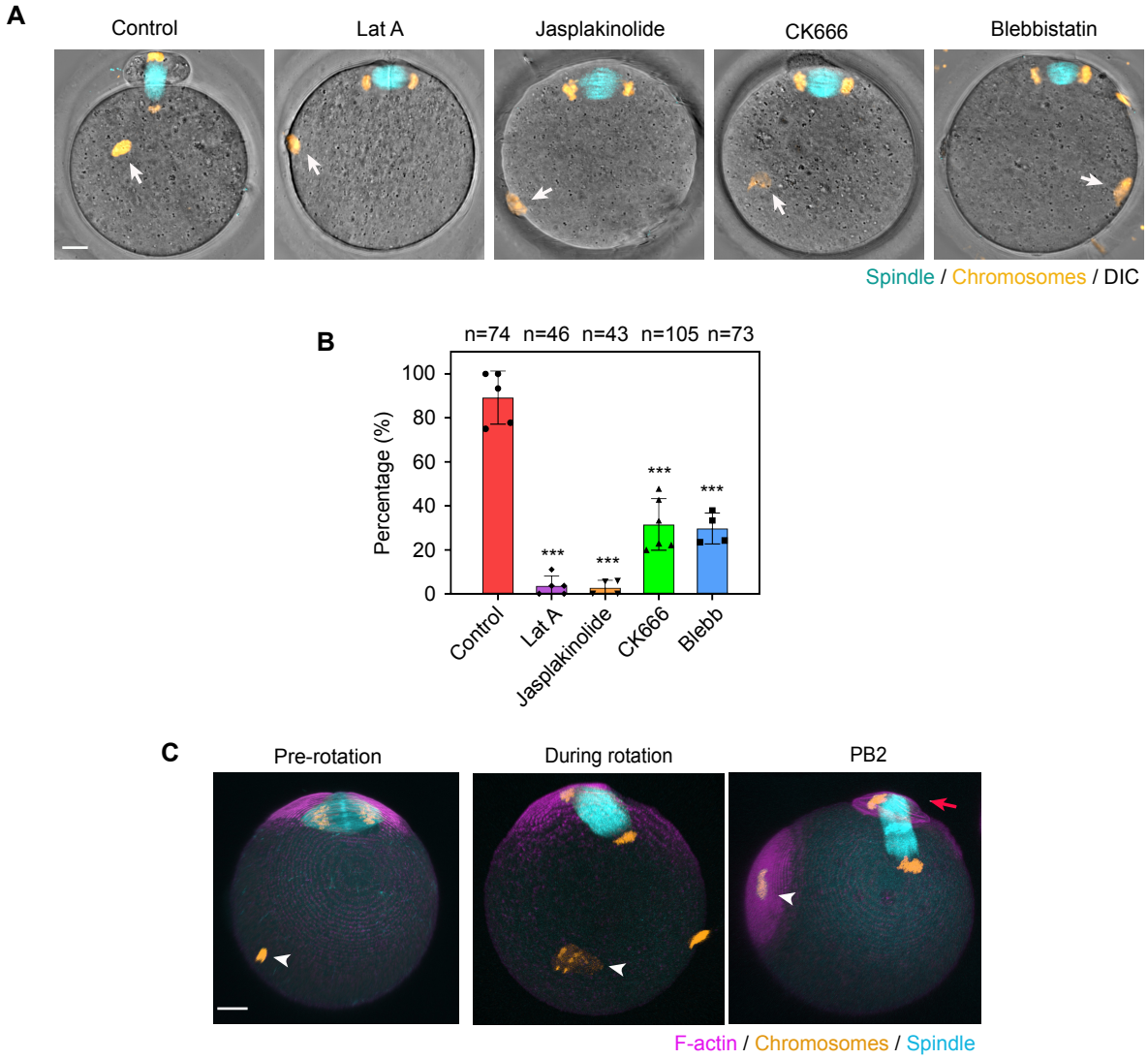

fig. S2. Spindle rotation in fertilized oocyte requires Arp2/3 complex, myosin-II and dynamic F-actin network.

(A) Inhibition of actin polymerization (Lat A treatment), actin depolymerization (jasplakinolide treatment), Arp2/3 complex (CK666 treatment) or myosin-II (blebbistatin treatment) prevented spindle rotation in the fertilized oocyte. Arrows indicate the sperm chromatin. **(B)** Quantification of spindle rotation percentage after various treatments as indicated. Data are mean ± SD. ***P < 0.001. n = oocytes number. **(C)** Immunofluorescence staining of F-actin (phalloidin), spindle (α-tubulin), and chromosomes (Hoechst) in oocytes after fertilization. White arrowheads indicate the paternal chromatin. Red arrow indicates the second polar body. Note that the mature FC actin cap formed only after PB2 formation. Scale bars for all images, 10 μm.

Figure S3

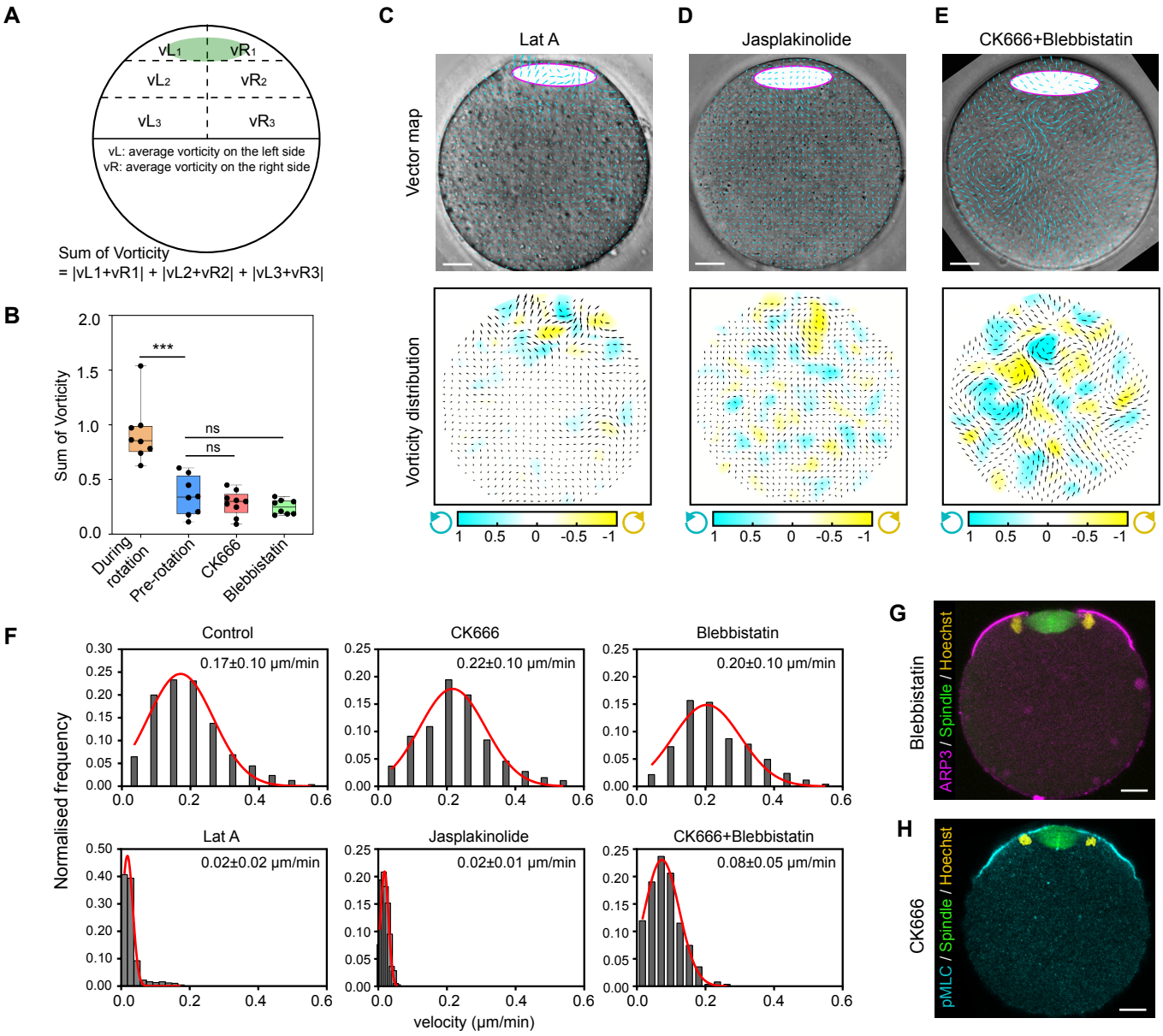
A
vL1
vR1
vL2
vR2
vL3
vR3
vL: average vorticity on the left side
vR: average vorticity on the right side
Sum of Vorticity
= |vL1+vR1| + |vL2+vR2| + |vL3+vR3|
B
Sum of Vorticity
***
ns
ns
During rotation
Pre-rotation
CK666
Blebbistatin
C
Lat A
D
Jasplakinolide
E
CK666+Blebbistatin
Vector map
Vorticity distribution
F
Control
CK666
Blebbistatin
Lat A
Jasplakinolide
CK666+Blebbistatin
0.17±0.10 μm/min
0.22±0.10 μm/min
0.20±0.10 μm/min
0.02±0.02 μm/min
0.02±0.01 μm/min
0.08±0.05 μm/min
Normalised frequency
velocity (μm/min)
G
Blebbistatin
ARP3 / Spindle / Hoechst
H
CK666
pMLC / Spindle / Hoechst

fig. S3. Observed cytoplasmic streaming patterns under various conditions.

(A), Schematics of the method for Sum of Vorticity (SOV) calculation. Note that a higher SOV means a greater asymmetric in vorticity between the left and right sides of the oocyte. **(B)**, Quantification of SOV in control (pre-rotation and during rotation), CK666-, or blebbistatin-treated oocytes. Note that pre-rotation flow has a small SOV similar to that in CK666- and blebbistatin-treated oocytes, whereas during-rotation flow SOV was significantly higher, indicating greater asymmetry. ***$P < 0.001$; ns, not significant. **(C to E),** Representative maps of velocity (top panels) and vorticity (bottom panels) of cytoplasmic flow in an actin polymerization- (C), depolymerization- (D) or dual Arp2/3 and myosin II-inhibited (E), oocyte analyzed by using PIV. Instant plots are shown. The color map in the bottom panel represents the normalized vorticity distribution, with blue and yellow tones representing counterclockwise and clockwise vorticity, respectively, as indicated in the color scale bar. White ellipses with magenta outline show the positions of spindle. **(F)** Histograms of instantaneous velocity of the cytoplasmic flow after various treatments as indicated. For each pattern, a Gaussian fit was applied (solid curve). The corresponding mean values from the fits are shown above the plots. **(G)** ARP3 distributions when myosin-II was inhibited by blebbistatin treatment. **(H)** Myosin-II distributions when Arp2/3 complex was inhibited by CK666 treatment. Scale bars for all images, 10 μm.

Figure S4

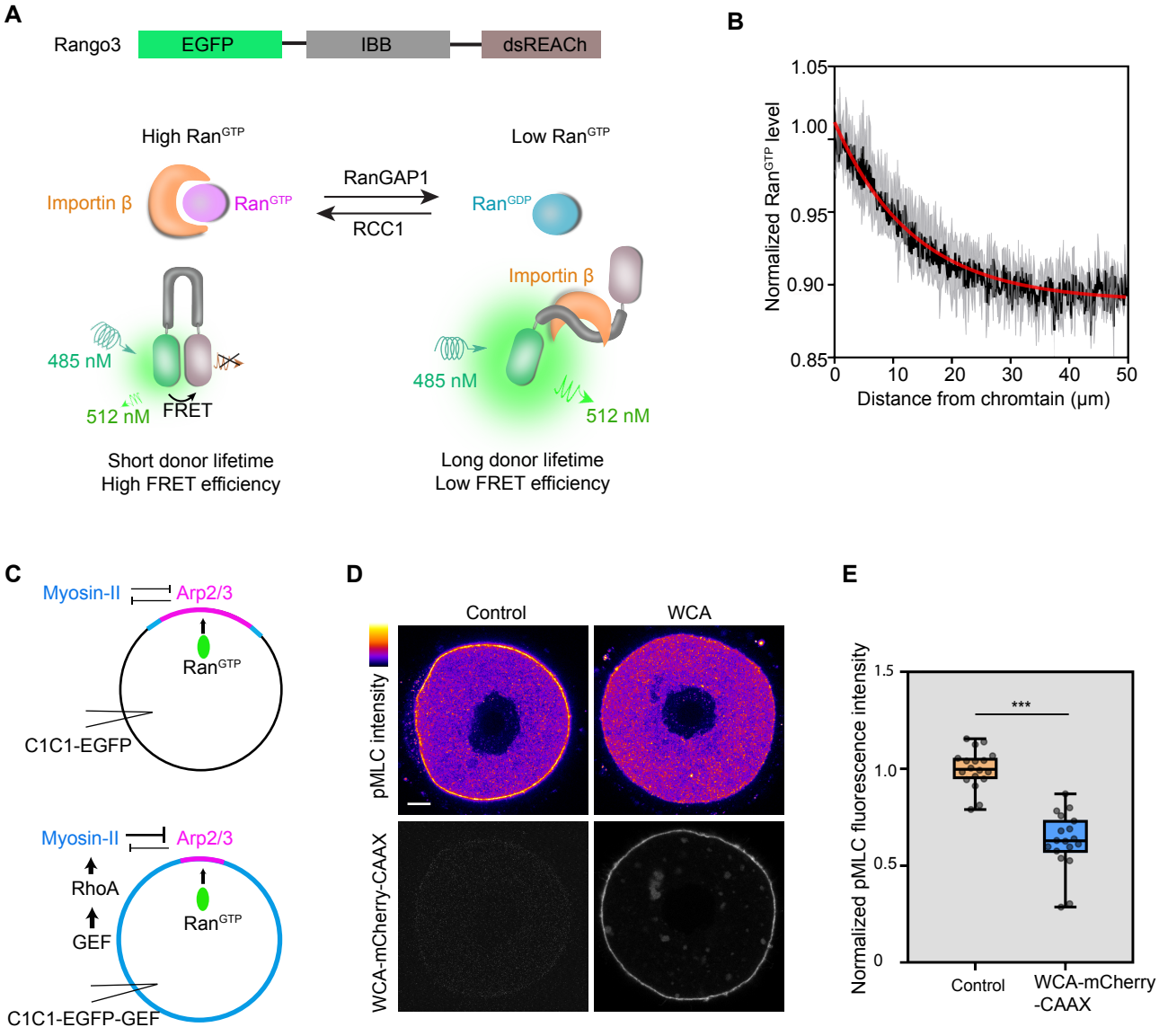
A
Rango3
EGFP
IBB
dsREACh
High Ran^GTP
Low Ran^GTP
Importin β
Ran^GTP
RanGAP1
RCC1
Ran^GDP
485 nM
512 nM
FRET
Short donor lifetime
High FRET efficiency
Importin β
485 nM
512 nM
Long donor lifetime
Low FRET efficiency
B
Normalized Ran^GTP level
1.05
1.00
0.95
0.90
0.85
0
10
20
30
40
50
Distance from chromtain (μm)
C
Myosin-II
Arp2/3
Ran^GTP
C1C1-EGFP
Myosin-II
Arp2/3
RhoA
GEF
Ran^GTP
C1C1-EGFP-GEF
D
Control
WCA
pMLC intensity
WCA-mCherry-CAAX
E
Normalized pMLC fluorescence intensity
1.5
1.0
0.5
0
***
Control
WCA-mCherry
-CAAX

fig. S4. Evidence for two feedback loops that could drive symmetry breaking during spindle rotation.

(A) Schematic explanation of the Rango-3 biosensor for Ran^{GTP} gradient. Rango-3 consists of importin β binding domain (IBB) flanked by the EGFP and the non-fluorescent dsREACh. Binding of importin β to Rango-3 sterically hinders the FRET interaction between EGFP and dsREACh. Where levels of Ran^{GTP} are high, the Ran^{GTP}-induced release of Rango from importin β relieves this steric hindrance, and FRET can occur, resulting in increased FRET and reduced EGFP fluorescence lifetime. **(B)** Normalized Ran^{GTP} level as a function of distance from chromosomes in anaphase II oocytes (n=6), with exponential fits (red line) giving length scale at half maximum of 9.3 μm. **(C)** Schematic explanation of the RhoGEF overexpression experiment. The result of this experiment is shown in Fig. 4h. **(D)** Representative immunofluorescence images of pMLC show that cortical Arp2/3 complex activation reduced myosin-II from the cortex. Scale bars, 10 μm. **(E)** Quantification of the averaged cortical pMLC fluorescence intensity after WCA-mCherry-CAAX overexpression. ***$P < 0.001$.

Figure S5

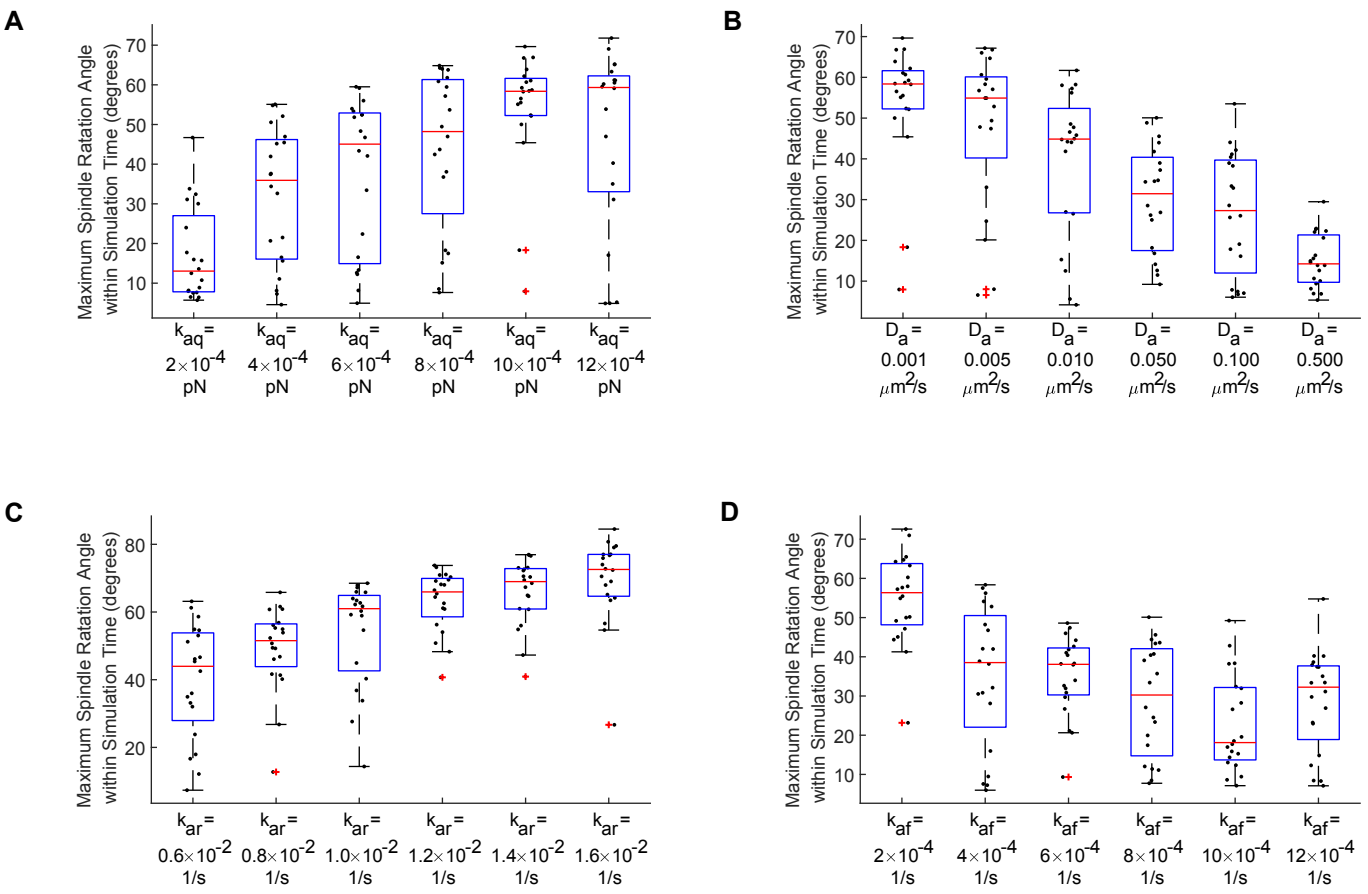

fig. S5. Sensitivity analysis for major model parameters.

(A) The impact of kaq, coefficient of effective Arp2/3 complex force, on the spindle rotation angle. **(B)** The impact of Da, diffusion coefficient of Arp2/3 complex, on the cortex on the spindle rotation angle. **(C)** The impact of kar, nucleation rate of Arp2/3 complex due to the Ran signal, on the spindle rotation angle. **(D)** The impact of kaf, off rate of Arp2/3 complex, on the spindle rotation angle. In each set of analysis in (A) - (D), we sweep one parameter (as indicated on the x-axes) and keep other parameters constant. Twenty simulations were run for each parameter. In each box plot, the central mark indicates the median, and the bottom and top edges of the box indicate the 25th and 75th percentiles, respectively. The whiskers extend to the most extreme data points not considered outliers, and the outliers are plotted individually using the '+' symbol.

Figure S6

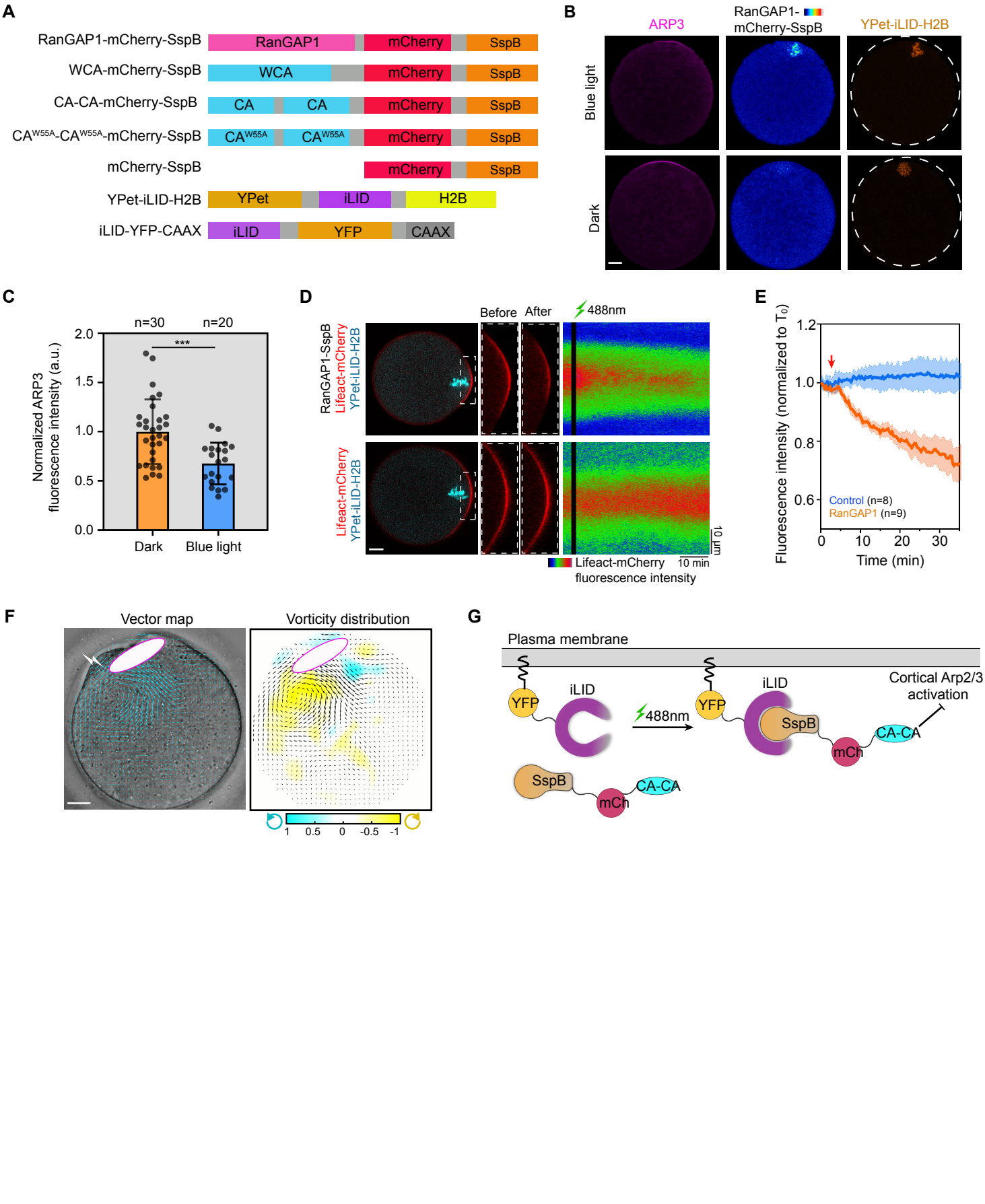
A
RanGAP1-mCherry-SspB
RanGAP1
mCherry
SspB
WCA-mCherry-SspB
WCA
CA-CA-mCherry-SspB
CA
CAW55A-CAW55A-mCherry-SspB
CAW55A
mCherry-SspB
YPet-iLID-H2B
YPet
iLID
H2B
iLID-YFP-CAAX
YFP
CAAX
B
ARP3
RanGAP1-mCherry-SspB
YPet-iLID-H2B
Blue light
Dark
C
n=30
n=20
***
Normalized ARP3 fluorescence intensity (a.u.)
Dark
Blue light
D
Before
After
488nm
RanGAP1-SspB
Lifeact-mCherry
YPet-iLID-H2B
10 μm
Lifeact-mCherry fluorescence intensity
10 min
E
Fluorescence intensity (normalized to T0)
Control (n=8)
RanGAP1 (n=9)
Time (min)
F
Vector map
Vorticity distribution
1
0.5
0
-0.5
-1
G
Plasma membrane
iLID
YFP
488nm
SspB
mCh
CA-CA
Cortical Arp2/3 activation

fig. S6. Optogenetic analysis for biasing spindle rotation.

(A) Schematic diagrams showing the constructs used for optogenetic experiments aimed to bias spindle rotation. **(B)** Oocytes expressing RanGAP1-SspB and YPet-iLID-H2B were illuminated using blue light and immunostained for ARP3. Dashed line indicates oocyte cortex. **(C)** Quantification of averaged ARP3 fluorescence intensity at cortical cap regain after blue light illuminates. ***P < 0.001. **(D)** Live imaging show optogenetic recruitment of RanGAP1 to the chromosomes disrupted actin cap assembly. Oocytes were injected with RanGAP1-SspB, YPet-iLID-H2B, and Lifeact-mCherry. Kymographs show Lifeact-mCherry dynamics following by illuminating the chromosomes with a 488 nm laser. **(E)** Lifeact fluorescence intensity at the cortical cap following optogenetic recruitment (arrow) of RanGAP1 to the chromatin cluster. Plots are mean (line) and SD (shade). **(F)** Characterization of cytoplasm flow in the oocyte shown in Fig. 6B analyzed by using PIV. Arrows are velocity vectors. White ellipses with magenta outline show the positions of spindle. **(G)** Schematic depiction of optogenetic targeting of CA-CA-mCherry-SspB to the plasma membrane. Related results are shown in Fig. 6g and 6f. Scale bars for all images, 10 μm.

Figure S7

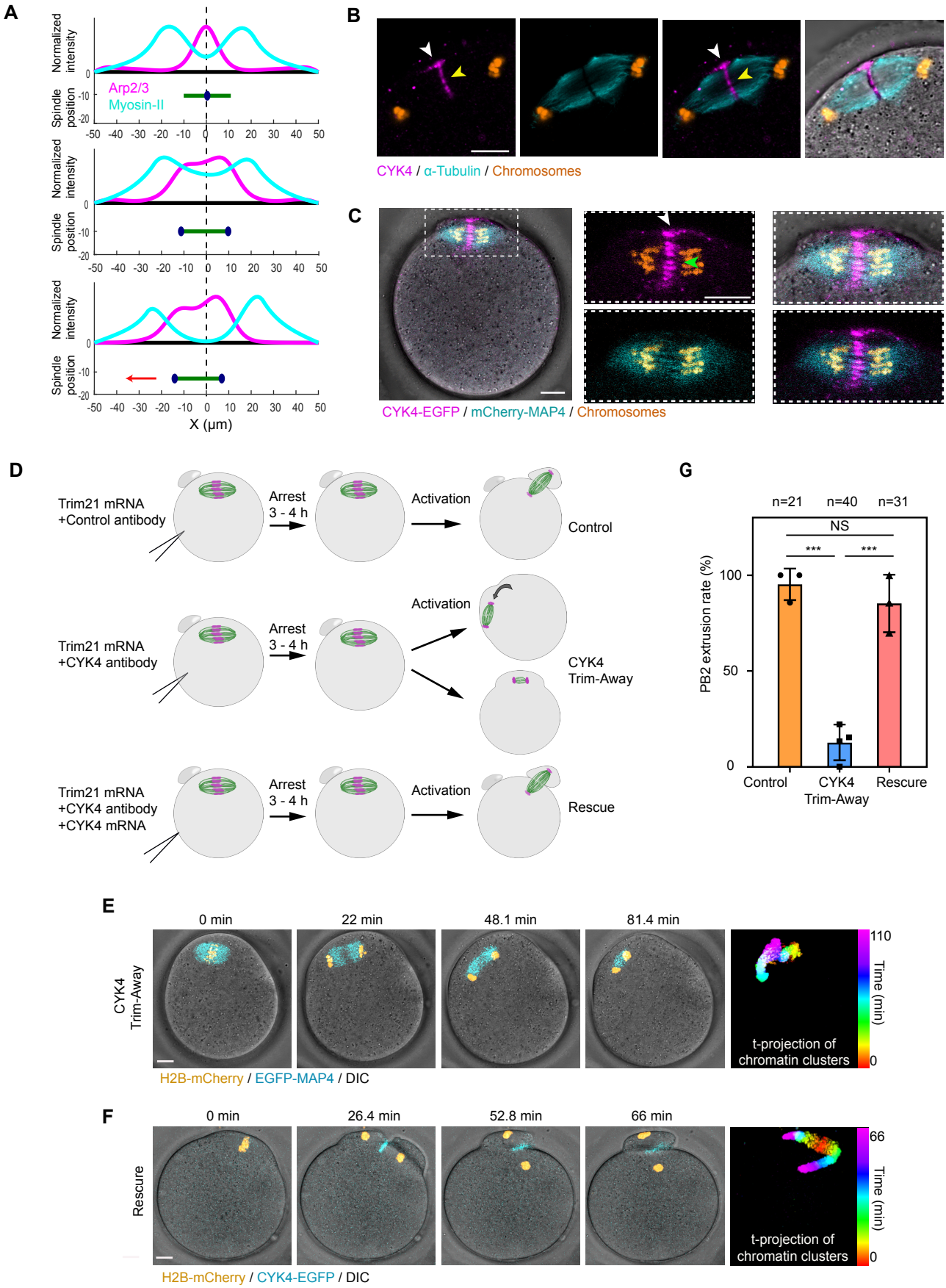
A
Normalized intensity
Arp2/3
Myosin-II
Spindle position
X (μm)
B
CYK4 / α-Tubulin / Chromosomes
C
CYK4-EGFP / mCherry-MAP4 / Chromosomes
D
Trim21 mRNA
+Control antibody
Arrest
3 - 4 h
Activation
Control
Trim21 mRNA
+CYK4 antibody
CYK4
Trim-Away
Trim21 mRNA
+CYK4 antibody
+CYK4 mRNA
Rescue
G
n=21
n=40
n=31
NS
***
PB2 extrusion rate (%)
Control
CYK4
Trim-Away
Rescure
E
0 min
22 min
48.1 min
81.4 min
CYK4
Trim-Away
t-projection of
chromatin clusters
Time (min)
H2B-mCherry / EGFP-MAP4 / DIC
F
0 min
26.4 min
52.8 min
66 min
Rescure
H2B-mCherry / CYK4-EGFP / DIC

Fig. S7. CYK4 Trim-Away and rescue experiments demonstrating the requirement for the anchor/pivot point in spindle rotation.

(A) Predictions on Arp2/3 complex and myosin-II distributions and spindle movement when the spindle is not anchored. **(B)** A representative immunofluorescence image showing that CYK4 accumulated at the spindle midzone (yellow arrowheads) and the contacting furrow membrane (white arrowheads) in a mouse oocyte after the completion of anaphase. Scale bar, 10 μm. **(C)** Live oocyte imaging showing that CYK4-EGFP, expressed via mRNA injection, accumulated at the spindle midzone (green arrowheads) and the contacting furrow membrane (white arrowheads). Scale bar, 10 μm. **(D)** Schematics of CYK4 Trim-Away and rescue experiments. **e,f** Montage from live imaging of an example showing collapsed anaphase spindle that did not rotate after CYK4 Trim-Away (D), as well as the rescue of spindle rotation by CYK4-EGFP mRNA injection (E). Oocytes were injected with mCherry-Trim21 mRNA, anti-CYK4 antibody, and EGFP-MAP4 (to label anaphase spindle). For rescue, CYK4-EGFP mRNA was injected together with anti-CYK4 antibody and mCherry-Trim21 mRNA. **(G)** Quantification of the frequency of the second polar body extrusion in control, CYK4 Trim-Away and rescue experiments. Data are mean ± SD. ***P < 0.001. Scale bar, 10 μm.

Figure S8

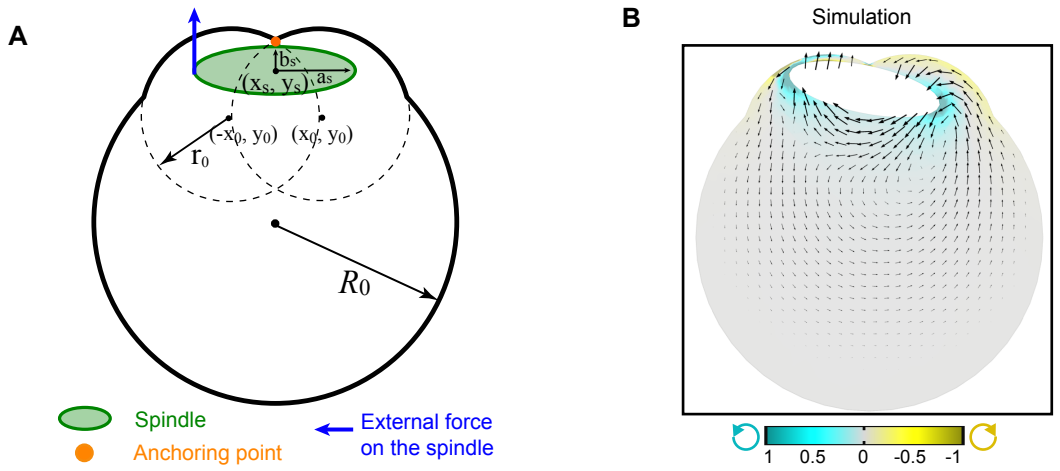

Fig. S8. Model simulation of cytoplasmic flow induced purely by spindle rotation.

(A) Diagram of the xy-plane of the 3D model showing the external force applied to the spindle. The spindle is anchored at the top but neither Arp2/3 complex nor myosin-II is present. **(B)** The spindle rotates as a result of the external force. The cytoplasmic fluid flows according to the motion of the spindle. The color map shows the strength of vorticity. Black arrows indicate the velocity of cytoplasmic flow. Longer arrows correspond to higher velocity amplitude. The flow pattern from the forced spindle rotation is different from the flow pattern generated from Arp2/3 complex and myosin II, suggesting that the observed follow pattern in the experiments results from Arp2/3 complex and myosin-II forcing, not from spindle rotation.

Table S1. Parameters used in the COMSOL model.

Parameters	**Physical Meanings**	**Values**
R_0 (μm)	Radius of the oocyte	36
r_0 (μm)	Radius of small protrusions	18
($\mp x_0$, y_0) (μm)	Center position of the protrusions	($\mp$8.5, 20)
(x_s, y_s) (μm)	Initial center position of the spindle	(0, 30.7)
a_s (μm)	Long semi-axis of the spindle	16
b_s (μm)	Short semi-axis of the spindle	5
d_1 (μm)	Horizontal distance limit of myosin-II distribution	9
d_2 (μm)	Horizontal distance of myosin-II separation	23
μ (Pa s)	Dynamic viscosity of the cytoplasm	0.01
ρ (kg/m^3)	Density of the cytoplasm	1000

Table S2. Parameters used in the symmetry breaking and spindle rotation model.

Parameters	Physical Meanings	Values
Δx (μm)	Spatial discretization of the computational domain	$\ell/50$
Δt (s)	Temporaldiscretization of the computational domain	0.1
d_0 (μm)	Distance from the center of the spindle to the cortex	6
ℓ (μm)	Half length of the computational domain	50
ℓ_s (μm)	Maximum separation distance of chromosomes	30
T_{s0} (min)	Starting time of chromosome separation	30
T_s (min)	Time course of chromosome separation	25
λ (μm)	Characteristic length of Ran signal gradient	9.32
β	Constant in Ran intensity	2.66
Ran^0	Maximum active Ran intensity (scaled)	1
D_m (μm^2/s)	Diffusion coefficient of myosin on the cortex	0.05
D_a (μm^2/s)	Diffusion coefficient of Arp2/3 complex on the cortex	0.005
k_{mf} (1/s)	Off rate of myosin	2×10^{-4}
k_{af} (1/s)	Off rate of Arp2/3 complex	2×10^{-4}
k_{ar} (1/s)	Ran-dependent activation rate of Arp2/3 complex	8×10^{-3}
k^0_{mo} (1/s)	Binding rate of myosin from the myosin in the cytoplasm	9×10^{-4}
k_{am} (1/s)	Inhibitory coefficient of Arp2/3 complex on myosin-II	2.4×10^{-3}
m_c	Average myosin intensity in the cytoplasm (scaled)	1
k_{aq} (nN/unit scaled intensity)	Coefficient of Arp2/3 complex-generated force	10×10^{-4}
k_{mq} (nN/unit scaled intensity)	Coefficient of myosin II-generated force	6×10^{-4}
η (μN·μm·s/rad)	Rotational viscosity of the spindle	600
k_{random}	Scaling factor for random torque	0.1

Notes for both Supplementary Table 1 and 2: The geometry-related parameters and parameters associated with the Ran gradient were obtained directly from experiments. The viscosity of the cytoplasm is taken as one order of magnitude higher than the viscosity of water in consideration

of the presence of actin network and other organelles within the cytoplasm. This estimation is based on the viscosity of actin network, which is 1 Pa·s (*55*, *56*), and the volume fraction of actin network within the cytoplasm, which is only about 1−2% (*57*). The density of the cytoplasm and the spindle are taken as the same as water because proteins or organelles typically have similar density of water (*58*). The parameters associated with Arp2/3 and myosin kinetics were estimated. It should be noted that relative ratios of kinetic parameters, instead of the absolute values, determine the dynamics of the system. For instance, the relative diffusion coefficients of myosin and Arp2/3 are more important than the absolute value for each. This can be seen from the parameter analysis. The length scale of the spatial pattern of Arp2/3 and myosin were determined by $\sqrt{D_{m,a}/k_{mf,af}}$. The combination of the parameters predicts the proper dynamic response of the spindle.

Table S3. Parameters used in the COMSOL model for absence of the anchor (pivot) point.

Parameters	**Physical Meanings**	**Values**
R_0 (μm)	Radius of the oocyte	36
r_0 (μm)	Radius of small protrusions	18
(x_s, y_s) (μm)	Initial center position of the spindle	(0, 29.5)
a_s (μm)	Long semi-axis of the spindle	11.55
b_s (μm)	Short semi-axis of the spindle	3.95
θ (degrees)	Asymmetry degree	5°
d_1 (μm)	Distance associated with myosin-II distribution	10
d_2 (μm)	Distance associated with Arp2/3 complex distribution	25
μ (Pa s)	Dynamic viscosity of the cytoplasm	0.01
ρ (kg/m^3)	Density of the cytoplasm	1000

Movie legends

Movie S1. Meiosis II spindle rotation occurs after anaphase onset.

Time-lapse imaging of an oocyte expressing mCherry-MAP4 (cyan), EGFP-CDK5RAP2 (magenta) and Hoechst (orange), merged with differential interference contrast (DIC) images of the oocyte. z projection of five sections, every 3 µm; time interval: 132s.

Movie S2. Dynamic actin is required for spindle rotation.

Live-cell time-lapse imaging of a Lat A (inhibition of actin polymerization) or jasplakinolide (inhibition of actin depolymerization) treated oocyte expressing EGFP-MAP4 (cyan) and H2B-mCherry (orange). z projection of five sections, every 3 µm; time interval: 132 s.

Movie S3. 3D reconstruction of ARP3 and myosin-II in the anaphase II oocyte prior to and during spindle rotation.

Fixed oocyte immunostained for ARP3 (magenta), myosin-II (pMLC, cyan), and chromosomes (Hoechst, green). 3D reconstructions were generated in Imaris from z stacks of 55 sections, every 1.5 µm.

Movie S4. Cytoplasmic flow before and during spindle rotation.

Time-lapse imaging of an oocyte expression H2B-mCherry (to label chromosomes). Cytoplasmic particles are visible under the DIC channel. Single confocal section; time interval: 60 s. The same oocyte was used for PIV analysis in Fig. 3a,b.

Movie S5. Inhibition of actin polymerization or depolymerization prevents spindle rotation.

Live-cell time-lapse imaging of a Lat A (inhibition of actin polymerization) or jasplakinolide (inhibition of actin depolymerization) treated oocyte showing cytoplasmic streaming are eliminated. Chromosomes were stained with Hoechst. Single confocal section; time interval: 132 s.

Movie S6. Cytoplasmic streaming in a myosin-II or Arp2/3 complex inhibited oocyte.

Time-lapse imaging of a blebbistatin-treated (inhibition of myosin-II) or CK666-treated (inhibition of Arp2/3 complex) oocyte showing cytoplasmic streaming remains bilaterally symmetric.

Cytoplasmic particles are visible under the DIC channel. Arrowheads in blebbistatin-treated oocyte show the positions of chromosomes. Single confocal section; time interval: 132 s.

Movie S7. A simulated movie shows cytoplasmic flow pattern produced by the asymmetric distribution of Arp2/3 complex and myosin-II.

Arrows indicate the velocity vectors of cytoplasmic flow; the color map represents the normalized vorticity distribution, with blue and yellow tones representing counterclockwise and clockwise vorticity, respectively. The xy-plane is shown where z = 0.

Movie S8. A simulated movie showing symmetry breaking in the cortical distribution of Arp2/3 complex and myosin-II.

Ran signal is symmetrically around each chromatin cluster. Cyan line, myosin-II; magenta line, Arp2/3; green line, spindle; blue dot, chromosomes.

Movie S9. A simulated movie showing biased rotation when Ran signal is partially inhibited.

Ran signal is partially inhibited at the left side of the chromosome cluster. This leads to a biased rotation of the spindle away from the side where Ran is partially inhibited. Cyan line, myosin-II; magenta line, Arp2/3; green line, spindle; blue dot, chromosomes.

Movie S10. Optogenetic recruitment of RanGAP1 to one of the chromatin clusters.

Oocytes were injected with YPet-iLID-H2B (heatmap) and RanGAP1-mCherry-SspB (cyan). The left side of the chromatin cluster was illuminated with 488nm wavelength. The recruitment of RanGAP1 is pointed by white arrow. Single confocal section; time interval: 30s.

Movie S11. Optogenetic recruitment of WCA domain to the cortical region adjacent to a chromatin cluster.

Oocytes were injected with WCA-mCherry-SspB (heatmap), iLID-YFP-CAAX (cyan), and YPet-H2B (to label chromosomes, cyan). The cortical region adjacent to the upper chromatin cluster was illuminated with 488nm wavelength. The recruitment of WCA is pointed out by white arrowhead. Chromatin clusters are pointed out by white arrows. Note the cyan cluster pointed by orange arrow resulted from the iLID-YFP-CAAX signal at furrow membrane. Single confocal section; time interval: 30s.

Movie S12. Optogenetic recruitment of CA-CA domain to the cortical region adjacent to a chromatin cluster.

Oocytes were injected with CA-CA-mCherry-SspB (heatmap), iLID-YFP-CAAX (cyan), and YPet-H2B (to label chromosomes, cyan). The cortical region adjacent to the lower chromatin cluster was illuminated with 488nm wavelength. The recruitment of CA-CA is pointed out by white arrowhead. Chromatin clusters are pointed out by white arrows. Note the cyan cluster pointed by orange arrow resulted from the iLID-YFP-CAAX signal at furrow membrane. Single confocal section; time interval: 30s.

Movie S13. Model simulated movies without the anchoring point.

Part 1, A simulated movie shows cytoplasmic flow and spindle drifts using the COMSOL model without an anchoring point. Arrows are the velocity vectors of the cytoplasmic flow. Part 2, A simulated movie from symmetry breaking model when the spindle is not anchored. Cyan line, myosin-II; magenta line, Arp2/3; green line, spindle; blue dot, chromosomes.

Movie S14. CYK4 Trim-Away induces anaphase spindle to move along the cortex.

In CYK4 Trim-Away experiment, oocytes were injected with Trim21 mRNA and anti-CYK4 antibody. Yellow shows the Hoechst staining of chromosomes. z projection of four sections, every 3 μm; time interval: 180 s. In the rescue experiment, CYK4-EGFP mRNA was co-injected with mCherry-Trim21 mRNA and CYK4 antibody into oocytes. z projection of five sections, every 3 μm; time interval: 132 s.

REFERENCES AND NOTES

1. X. Morin, Y. Bellaïche, Mitotic spindle orientation in asymmetric and symmetric cell divisions during animal development. *Dev. Cell* **21**, 102–119 (2011).

2. R. Li, The art of choreographing asymmetric cell division. *Dev. Cell* **25**, 439–450 (2013).

3. C. G. Pearson, K. Bloom, Dynamic microtubules lead the way for spindle positioning. *Nat. Rev. Mol. Cell Biol.* **5**, 481–492 (2004).

4. F. di Pietro, A. Echard, X. Morin, Regulation of mitotic spindle orientation: An integrated view. *EMBO Rep.* **17**, 1106–1130 (2016).

5. R. Li, D. F. Albertini, The road to maturation: Somatic cell interaction and self-organization of the mammalian oocyte. *Nat. Rev. Mol. Cell Biol.* **14**, 141–152 (2013).

6. D. Clift, M. Schuh, Restarting life: Fertilization and the transition from meiosis to mitosis. *Nat. Rev. Mol. Cell Biol.* **14**, 549–562 (2013).

7. D. Szollosi, P. Calarco, R. P. Donahue, Absence of centrioles in the first and second meiotic spindles of mouse oocytes. *J. Cell Sci.* **11**, 521–541 (1972).

8. D. Clift, M. Schuh, A three-step MTOC fragmentation mechanism facilitates bipolar spindle assembly in mouse oocytes. *Nat. Commun.* **6**, 7217 (2015).

9. Z. Holubcová, M. Blayney, K. Elder, M. Schuh, Human oocytes. Error-prone chromosome-mediated spindle assembly favors chromosome segregation defects in human oocytes. *Science* **348**, 1143–1147 (2015).

10. A. Chaigne, C. Campillo, N. S. Gov, R. Voituriez, J. Azoury, C. Umaña-Diaz, M. Almonacid, I. Queguiner, P. Nassoy, C. Sykes, M.-H. Verlhac, M.-E. Terret, A soft cortex is essential for asymmetric spindle positioning in mouse oocytes. *Nat. Cell Biol.* **15**, 958–966 (2013).

11. M. Schuh, An actin-dependent mechanism for long-range vesicle transport. *Nat. Cell Biol.* **13**, 1431–1436 (2011).

12. K. Yi, B. Rubinstein, J. R. Unruh, F. Guo, B. D. Slaughter, R. Li, Sequential actin-based pushing forces drive meiosis I chromosome migration and symmetry breaking in oocytes. *J. Cell Biol.* **200**, 567–576 (2013).

13. K. Yi, J. R. Unruh, M. Deng, B. D. Slaughter, B. Rubinstein, R. Li, Dynamic maintenance of asymmetric meiotic spindle position through Arp2/3-complex-driven cytoplasmic streaming in mouse oocytes. *Nat. Cell Biol.* **13**, 1252–1258 (2011).

14. M. Deng, P. Suraneni, R. M. Schultz, R. Li, The Ran GTPase mediates chromatin signaling to control cortical polarity during polar body extrusion in mouse oocytes. *Dev. Cell* **12**, 301–308 (2007).

15. Q. Wang, C. Racowsky, M. Deng, Mechanism of the chromosome-induced polar body extrusion in mouse eggs. *Cell Div* **6**, 17 (2011).

16. S. Matson, S. Markoulaki, T. Ducibella, Antagonists of myosin light chain kinase and of myosin II inhibit specific events of egg activation in fertilized mouse eggs. *Biol. Reprod.* **74**, 169–176 (2006).

17. G. Halet, J. Carroll, Rac activity is polarized and regulates meiotic spindle stability and anchoring in mammalian oocytes. *Dev. Cell* **12**, 309–317 (2007).

18. B. Dehapiot, V. Carrière, J. Carroll, G. Halet, Polarized Cdc42 activation promotes polar body protrusion and asymmetric division in mouse oocytes. *Dev. Biol.* **377**, 202–212 (2013).

19. M. H. Kaufman, L. Sachs, The early development of haploid and aneuploid parthenogenetic embryos. *J. Embryol. Exp. Morphol.* **34**, 645–655 (1975).

20. B. E. Rosenbusch, Mechanisms giving rise to triploid zygotes during assisted reproduction. *Fertil. Steril.* **90**, 49–55 (2008).

21. Z.-Y. Zhu, D.-Y. Chen, J.-S. Li, L. Lian, L. Lei, Z.-M. Han, Q.-Y. Sun, Rotation of meiotic spindle is controlled by microfilaments in mouse oocytes. *Biol. Reprod.* **68**, 943–946 (2003).

22. B. Maro, M. H. Johnson, S. J. Pickering, G. Flach, Changes in actin distribution during fertilization of the mouse egg. *J. Embryol. Exp. Morphol.* **81**, 211–237 (1984).

23. B. J. Nolen, N. Tomasevic, A. Russell, D. W. Pierce, Z. Jia, C. D. McCormick, J. Hartman, R. Sakowicz, T. D. Pollard, Characterization of two classes of small molecule inhibitors of Arp2/3 complex. *Nature* **460**, 1031–1034 (2009).

24. A. F. Straight, A. Cheung, J. Limouze, I. Chen, N. J. Westwood, J. R. Sellers, T. J. Mitchison, Dissecting temporal and spatial control of cytokinesis with a myosin II Inhibitor. *Science* **299**, 1743–1747 (2003).

25. J. Tao, S. X. Sun, Active biochemical regulation of cell volume and a simple model of cell tension response. *Biophys. J.* **109**, 1541–1550 (2015).

26. R. Li, G. G. Gundersen, Beyond polymer polarity: How the cytoskeleton builds a polarized cell. *Nat. Rev. Mol. Cell Biol.* **9**, 860–873 (2008).

27. A. B. Goryachev, M. Leda, Many roads to symmetry breaking: Molecular mechanisms and theoretical models of yeast cell polarity. *Mol. Biol. Cell* **28**, 370–380 (2017).

28. J. Xu, F. Wang, A. Van Keymeulen, P. Herzmark, A. Straight, K. Kelly, Y. Takuwa, N. Sugimoto, T. Mitchison, H. R. Bourne, Divergent signals and cytoskeletal assemblies regulate self-organizing polarity in neutrophils. *Cell* **114**, 201–214 (2003).

29. A. J. Lomakin, K.-C. Lee, S. J. Han, D. A. Bui, M. Davidson, A. Mogilner, G. Danuser, Competition for actin between two distinct F-actin networks defines a bistable switch for cell polarization. *Nat. Cell Biol.* **17**, 1435–1445 (2015).

30. J. F. Soderholm, S. L. Bird, P. Kalab, Y. Sampathkumar, K. Hasegawa, M. Uehara-Bingen, K. Weis, R. Heald, Importazole, a small molecule inhibitor of the transport receptor importin-β. *ACS Chem. Biol.* **6**, 700–708 (2011).

31. P. Kalab, R. Heald, The RanGTP gradient–A GPS for the mitotic spindle. *J. Cell Sci.* **121**, 1577–1586 (2008).

32. E. Wagner, M. Glotzer, Local RhoA activation induces cytokinetic furrows independent of spindle position and cell cycle stage. *J. Cell Biol.* **213**, 641–649 (2016).

33. S. Lekomtsev, K.-C. Su, V. E. Pye, K. Blight, S. Sundaramoorthy, T. Takaki, L. M. Collinson, P. Cherepanov, N. Divecha, M. Petronczki, Centralspindlin links the mitotic spindle to the plasma membrane during cytokinesis. *Nature* **492**, 276–279 (2012).

34. W. Cho, Membrane targeting by C1 and C2 domains. *J. Biol. Chem.* **276**, 32407–32410 (2001).

35. K. G. Campellone, M. D. Welch, A nucleator arms race: Cellular control of actin assembly. *Nat. Rev. Mol. Cell Biol.* **11**, 237–251 (2010).

36. A. Chaigne, C. Campillo, N. S. Gov, R. Voituriez, C. Sykes, M. H. Verlhac, M. E. Terret, A narrow window of cortical tension guides asymmetric spindle positioning in the mouse oocyte. *Nat. Commun.* **6**, 6027 (2015).

37. G. Guntas, R. A. Hallett, S. P. Zimmerman, T. Williams, H. Yumerefendi, J. E. Bear, B. Kuhlman, Engineering an improved light-induced dimer (iLID) for controlling the localization and activity of signaling proteins. *Proc. Natl. Acad. Sci. U.S.A.* **112**, 112–117 (2015).

38. H. N. Higgs, L. Blanchoin, T. D. Pollard, Influence of the C terminus of Wiskott-Aldrich syndrome protein (WASp) and the Arp2/3 complex on actin polymerization. *Biochemistry* **38**, 15212–15222 (1999).

39. S. B. Padrick, H.-C. Cheng, A. M. Ismail, S. C. Panchal, L. K. Doolittle, S. Kim, B. M. Skehan, J. Umetani, C. A. Brautigam, J. M. Leong, M. K. Rosen, Hierarchical regulation of WASP/WAVE proteins. *Mol. Cell* **32**, 426–438 (2008).

40. D. Clift, W. A. McEwan, L. I. Labzin, V. Konieczny, B. Mogessie, L. C. James, M. Schuh, A method for the acute and rapid degradation of endogenous proteins. *Cell* **171**, 1692–1706.e18 (2017).

41. A. Ajduk, T. Ilozue, S. Windsor, Y. Yu, K. B. Seres, R. J. Bomphrey, B. D. Tom, K. Swann, A. Thomas, C. Graham, M. Zernicka-Goetz, Rhythmic actomyosin-driven contractions induced by sperm entry predict mammalian embryo viability. *Nat. Commun.* **2**, 417 (2011).

42. D. W. McLay, H. J. Clarke, Remodelling the paternal chromatin at fertilization in mammals. *Reproduction* **125**, 625–633 (2003).

43. R. E. Braun, Packaging paternal chromosomes with protamine. *Nat. Genet.* **28**, 10–12 (2001).

44. P. Sassone-Corsi, Unique chromatin remodeling and transcriptional regulation in spermatogenesis. *Science* **296**, 2176–2178 (2002).

45. S. D. Perreault, Chromatin remodeling in mammalian zygotes. *Mutat. Res.* **296**, 43–55 (1992).

46. S. Nonchev, R. Tsanev, Protamine-histone replacement and DNA replication in the male mouse pronucleus. *Mol. Reprod. Dev.* **25**, 72–76 (1990).

47. M. E. Nemergut, C. A. Mizzen, T. Stukenberg, C. D. Allis, I. G. Macara, Chromatin docking and exchange activity enhancement of RCC1 by histones H2A and H2B. *Science* **292**, 1540–1543 (2001).

48. M. Deng, R. Li, Sperm chromatin-induced ectopic polar body extrusion in mouse eggs after ICSI and delayed egg activation. *PLOS One* **4**, e7171 (2009).

49. B. Goldstein, I. G. Macara, The PAR proteins: Fundamental players in animal cell polarization. *Dev. Cell* **13**, 609–622 (2007).

50. M. Mittasch, P. Gross, M. Nestler, A. W. Fritsch, C. Iserman, M. Kar, M. Munder, A. Voigt, S. Alberti, S. W. Grill, M. Kreysing, Non-invasive perturbations of intracellular flow reveal physical principles of cell organization. *Nat. Cell Biol.* **20**, 344–351 (2018).

51. S. Kishigami, T. Wakayama, Efficient strontium-induced activation of mouse oocytes in standard culture media by chelating calcium. *J. Reprod. Dev.* **53**, 1207–1215 (2007).

52. W. Thielicke, E. J. Stamhuis, PIVlab-towards user-friendly, affordable and accurate digital particle image velocimetry in MATLAB. *J. Open Res. Softw.* **2**, e30 (2014).

53. Y. Zheng, A membranous spindle matrix orchestrates cell division. *Nat. Rev. Mol. Cell Biol.* **11**, 529–535 (2010).

54. M. Caudron, G. Bunt, P. Bastiaens, E. Karsenti, Spatial coordination of spindle assembly by chromosome-mediated signaling gradients. *Science* **309**, 1373–1376 (2005).

55. T. Kim, M. L. Gardel, E. Munro, Determinants of fluidlike behavior and effective viscosity in cross-linked actin networks. *Biophys. J.* **106**, 526–534 (2014).

56. K. S. Zaner, T. P. Stossel, Some perspectives on the viscosity of actin filaments. *J. Cell Biol.* **93**, 987–991 (1982).

57. R. L. Satcher Jr., C. F. Dewey Jr., Theoretical estimates of mechanical properties of the endothelial cell cytoskeleton. *Biophys. J.* **71**, 109–118 (1996).

58. R. Milo, R. Phillips, N. Orme, *Cell Biology by the Numbers* (Garland Science, Taylor & Francis Group, 2016).